JEM

Journal of Electron Microscopy **61(3)**: 145–157 (2012)
doi: 10.1093/jmicro/dfs038

Physical: Full-length

Local symmetry breaking of a thin crystal structure of β-Si_3N_4 as revealed by spherical aberration corrected high-resolution transmission electron microscopy images

Hwang Su Kim[1,*], Zaoli Zhang[2,3,*] and Ute Kaiser[2,*]

[1]Department of Physics, Kyungsung University, Busan 608-736, Republic of Korea, [2]Materials Science Electron Microscopy, Ulm University, 89060 Ulm, Germany and [3]Erich Schmid Institute of Materials Science, Austrian Academy of Sciences, A-8700 Leoben, Austria
*To whom correspondence should be addressed. E-mail: jwa@ks.ac.kr, zaoli.zhang@ceaw.ac.at, ute.kaiser@uni-ulm.de

Abstract This report is an extension of the study for structural imaging of 5–6 nm thick β-Si_3N_4 [0001] crystal with a spherical aberration corrected transmission electron microscope by Zhang and Kaiser [2009. Structure imaging of β-Si_3N_4 by spherical aberration-corrected high-resolution transmission electron microscopy. *Ultramicroscopy* 109, 1114–1120]. In this work, a local symmetry breaking with an uneven resolution of dumbbells in the six-membered rings revealed in the reported images in the study of Zhang and Kaiser has been analyzed in detail. It is found that this local asymmetry in the image basically is not relevant to a slight mistilt of the specimen and/or a beam tilt (coma). Rather the certain variation of the tetrahedral bond length of Si–N(4) in the crystal structure is found to be responsible for the uneven resolution with a local structural variation from region to region. This characteristic of the variation is also supposed to give a distorted lattice of apparently 2°–2.5° deviations from the perfect hexagonal unit cell as observed in the reported image in the work of Zhang and Kaiser. It is discussed that this variation may prevail only in a thin specimen with a thickness ranging ∼≤5–6 nm. At the same time, it is noted that the average of the bond length variation is close to the fixed length known in a bulk crystal of β-Si_3N_4.

Keywords atomic-resolution transmission electron microscopy, silicon nitride, microstructure, exit-wave reconstruction

Received 26 January 2012, accepted 14 February 2012; online 11 April 2012

Introduction

In a recent high-resolution transmission electron microscopy (HRTEM) study of β-Si_3N_4 [1], the high-resolution image at $C_s \sim 0$ and $\Delta f \sim 0$ using a 300 kV FEI Titan (80–300) as shown in Fig. 5b of Ref. [1] clearly showed the isolated nitrogen atom columns as well as Si–N dumbbells separated by 0.095 nm along the [0001] projection. Contrast details have been discussed in [1] and it was found that not all dumbbells in a six-membered ring were resolved with the same resolution, which was assumed to originate from a slight misorientation of the sample from the [0001] projection and/or residual aberrations.

The main purpose of this work was to find out the reason, which caused the uneven resolution over the field of view of the TEM image: whether this observation is due really to a slight misorientaion or the effect of specimen bending and/or residual aberrations of the microscope, or alternatively to an

intrinsic property of the structure with a possible local breaking of symmetry. In addition, we will discuss whether the intensity or phase images of the exit-surface plane wave reconstructed from the through-focal series of the high-resolution images shows better resolution. Further, we will demonstrate that the digital data of the exit-wave diffraction amplitudes can be used for the least-squares refinements of parameters of a model structure. For the exit-wave reconstruction, the iterative wave-function reconstruction (IWFR) method developed by Allen *et al.* [2,3] will be used with the four images shown in Fig. 3a–d of Ref. [1]. Employing this method in this case can be justified from a recent report [4]. This report, dealing with the specimen of β-$S_{i3}N_4$ [0001] with an ~7 nm thickness, has clearly shown that the IWFR method works very well for the retrieval of the exit-wave even when using only 4–5 images of an HRTEM focal series. The successful reconstruction of the exit-wave in this work can also be seen in Fig. 3.

Methods

Instruments and samples

The experiments were carried out using an FEI Titan (80–300) with a field-emission gun and an objective lens aberration corrector. All HRTEM images were taken on a 1024 × 1024 pixel CCD camera at a magnification of 1.4M, 1.25M and 620K. Si_3N_4 polycrystalline ceramics with a composition of Si_3N_4–2MgO–7.2La_2O_3 (in wt.%) were employed for atomic imaging, and some large Si_3N_4 grains were chosen for structural imaging [1].

Image simulations and analysis

Investigation of effects of specimen bending and residual aberrations

In order to see the effects of slight misorientation of the specimen bending and residual aberrations on the images, corresponding image simulations were carried out first. For calculations of images at the exit-surface of the specimen, the Howie–Whelan equation [5], equivalent to the Bloch wave method, was used. A possible bending of the specimen can be assumed to have been composed approximately of small, thin crystal slabs, with a continuous variation in local orientation slightly away from the zone axis. The coefficients of residual aberrations measured by Zhang and Kaiser [1] were used in the simulation, as well as the coherent wave aberration function as in Refs. [6,7]. All these simulations showed that the slight bending of the specimen approximated as a few milli-radian specimen tilting and/or the residual aberrations in Table 1 of Ref. [1] do not give a significant effect on the images of uneven resolution of dumbbells as shown in Fig. 1a (same as Fig. 5b of [1]). In addition, the residual aberrations listed in Table 1 of [8] for TEAM 0.5 at 300 kV were also examined to see their significant effects on the images. This list includes a second-order axial coma of $B_2 = 38$ nm and a fifth-order spherical aberration of $C_5 = 5.1$ mm. Calculations showed that these values give ±18° and 9° phase shifts in the phase-transfer function associated with the amplitude of the exit-wave, respectively, for the maximum g value of 10 nm^{-1}. Moreover, these are corresponding to the defocus values of ±0.5 and ~0.25 nm, respectively, for $g = 10$ nm^{-1} in the function. Thus, the effect of these aberrations on the images will be small. Indeed, the image simulations including all the data in Table 1 of Ref. [8] showed no significant changes in images in our case.

Asymmetry of images

A careful examination of the symmetry of the image and the pattern presented in Fig. 1a and b, respectively, reveals quite clearly the breaking of the hexagonal lattice symmetry. In Fig. 1a, the 4 × 4 unit cells (3.04 nm × 2.63 nm with dotted lines) show a deviation of ~2.5° from the hexagonal symmetry and therefore represent themselves as triclinic cells. In Fig. 1b, which is the fast Fourier transform (FFT) of Fig. 1a, this fact is easily seen by the deviation and splitting of spots.

It is important to note that the spots in Fig. 1b are split in various directions and do not form well-defined (reciprocal) lattice arrays. This fact indicates that the orientations and parameters of the triclinic cells vary slightly from region to region as shown in Fig. 1a. The origin of this peculiarity of the local structural variation in the images will be explored extensively in the subsequent sections.

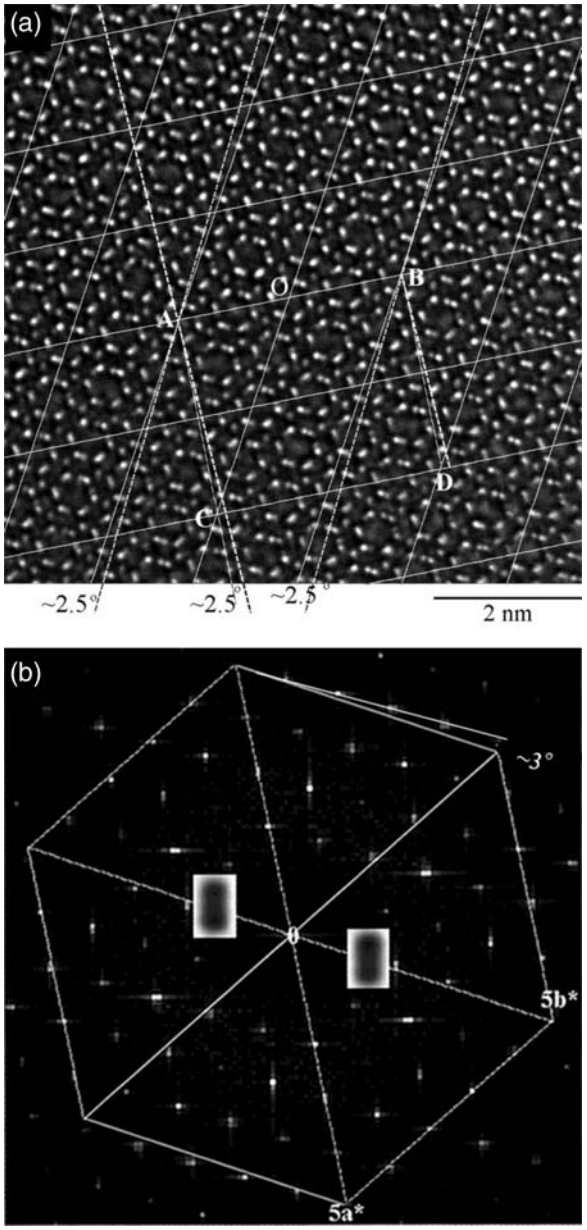

Fig. 1. (a) The experimental image of β-Si_3N_4[0001] taken under C_s = –0.5 μm at close to zero defocus (exact focus), (b) FFT of (a). In (a), the imposed faint solid lines represent a hexagonal network of 2 × 2 unit cells of a perfect crystal of β-Si_3N_4[0001], and the dotted lines represent the real lattice cell of a triclinic slightly deviated from the hexagonal by an angle of ~2.5°. The point at O is the common origin of the hexagonal and triclinic cells, and the rectangular ABCD contains the 4 × 4 perfect hexagonal unit cells (3.04 nm × 2.63 nm). In (b), a hexagon with equilateral triangles is drawn in order to see clearly the deviation of the reciprocal lattice spots from the hexagonal cell. The splitting spots in insets corresponding to spots at ±02.0 are enlarged five times for clarity. The splitting angle of these spots is measured by ~3°. $|5a^*| = |5b^*| = 1/(0.132\ \text{nm})$.

Image simulations and the exit-surface wave reconstruction

To obtain more structural information, the exit-wave reconstruction was performed using the four HRTEM images of Fig. 5 of Ref. [1] taken at different defoci. The intention was to prove, first, whether the exit-surface wave gives a better-resolved structural image than Fig. 1a. To perform the exit-wave reconstruction, data of accurate defocus values are required for each image. The true atomic structure of the observed images with the asymmetry as seen in Fig. 1a is completely unknown but supposed to have a similar form as the β-Si_3N_4 crystal structure. Therefore, it can be assumed that the averaged structure, imposed forcefully the translation and hexagonal lattice symmetries, would become close to the crystal structure of β-Si_3N_4. Since the crystal structure of a perfect β-Si_3N_4 crystal is well known [9,10], the exact defocus values at the exit-surface can be determined by matching the simulated and symmetrically averaged images. The result is shown in Fig. 2.

The images presented in Fig. 2a are parts of Fig. 5 of Ref. [1] with the 4 × 4 unit cells (3.04 nm × 2.63 nm). These images were taken from the rectangular area ABCD in Fig. 1a. The ABCD image itself is the same as the second one in Fig. 2a. Clearly, these images do not have the exact hexagonal lattice symmetry because the bottom is shifted from the top by ~2.5° toward left in the horizontal line. The images in Fig. 2b are the averaged images of Fig. 2a, giving the hexagonal lattice symmetry. This imaging process involved the following steps: first, the pixel points in the images of Fig. 2a were shifted by 2.5° in the horizontal line to make approximately a hexagonal lattice. Second, this lattice image was divided into 4 × 2 cells to do lattice translation averaging. Each cell is a supercell with twice the size of a hexagonal unit cell and is supposed to have the lattice translation symmetry. It should be noted that averaged images by this translation symmetry are essentially the same as the originally observed images except slight changes in cell shape. Finally, the averaging of 6-fold rotation symmetry of the images was done. These final, averaged images have perfect hexagonal lattice symmetry, as shown in Fig. 2b. Figure 2c presents simulated images that are in agreement with that of Fig. 2b for the following input data: the fixed C_s = –0.5 μm for a 300 kV TEM; the defocus values listed on the left of the figure; the specimen thickness, t = 5 nm; the Gaussian focus spread, Δ_s =

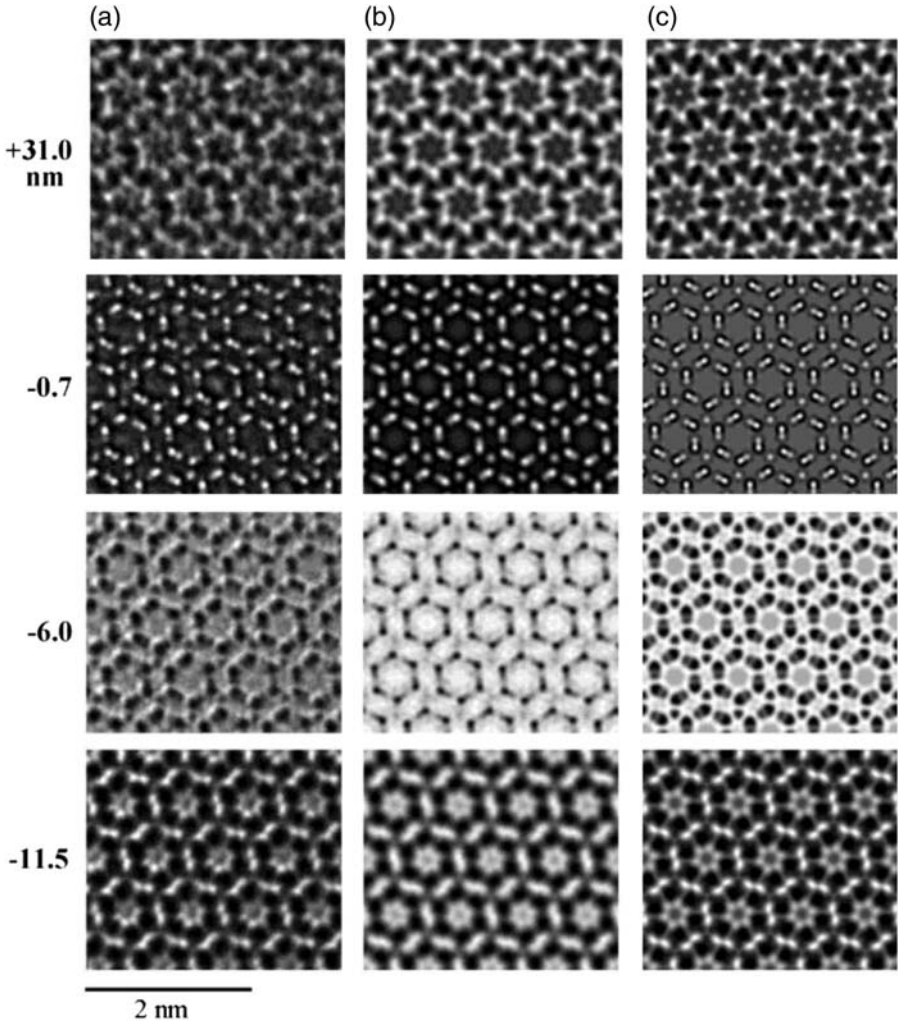

Fig. 2. (a) Observed HRTEM images at the defocus listed on the left side, (b) the averaged images imposed the hexagonal symmetry, (c) the simulated images corresponding to (b) images. For the image processing procedure from (a) images to (b), see text.

2.9 nm; and the semi-angle of the beam convergence, $\beta_s = 0.2$ mrad. It is seen that the agreement in the pattern between the simulated and observed images is generally good. Nevertheless, there are certain contrast mismatches between images in Fig. 2b and c. The reason for the contrast mismatches may be due to the well-known 'Stobbs-factor problem' [11] including the negligence of the detector modulation-transfer function in our image simulations [12]. It should also be noted that the averaged images in Fig. 2b did not come exactly from the true structure of the specimen. Thus, theoretically, it is not necessary to have an exact match between the images in Fig. 2b and c. Here, we emphasize that the purpose of this matching work is mainly to determine the exact defoci which are used in the exit-wave reconstruction from the experimental images. Therefore, this quantitative contrast mismatch is not considered as a serious problem in image matching.

Figure 3 displays the intensity and phase images of the exit-surface wave: Fig. 3a shows the reconstructed images of the exit-surface wave using the four images processed up to the second stage explained above, and, therefore, it has cell translation symmetry. Figure 3b represents the images using the four images in Fig. 2b, which have hexagonal lattice symmetry. Figure 3c represents the simulated images of the exit-surface plane wave of a perfect β-Si_3N_4 crystal with a thickness of 5 nm at $C_s = \Delta f = \Delta_s = \beta_s = 0.0$, but $g \leq 10\ \mathrm{nm}^{-1}$ limited by the objective aperture. In this reconstruction process, the image data at $\Delta f = -0.7$ nm in Fig. 2 was given the weight factor of 4 and others equally of 1. In

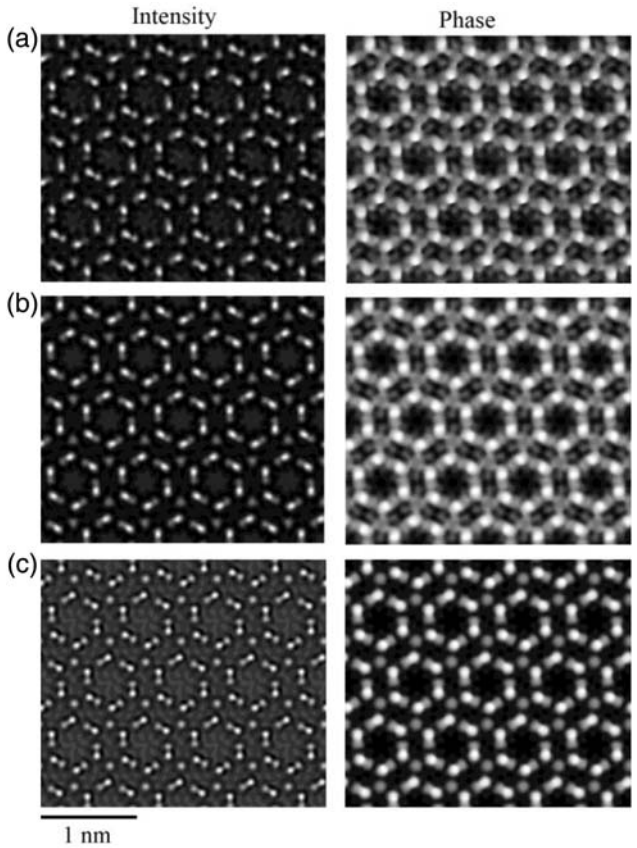

Fig. 3. (a) The intensity and the phase images of the exit-surface plane wave reconstructed from the images modified by image-processing with images in Fig. 2a, (b) the averaged images imposed the hexagonal symmetry and (c) the simulated images of the exit-surface plane wave. For more details, see text.

this way, a better-resolved intensity image of Fig. 3a than that of the image at $\Delta f = -0.7$ nm in Fig. 2a was obtained.

This improvement of resolution can further be confirmed by comparing the symmetrically averaged intensity image of Fig. 3b with that at $\Delta f = -0.7$ nm in Fig. 2b. Now, it can be seen that in the intensity image of Fig. 3b, the measured separations of the Si–N dumbbells in the six-membered rings are very close to the true separations of the atomic columns along the [0001]-direction (see Table 2).

FFTs of the exit-surface wave and the intensity

Figure 4a shows the map of the amplitudes of the FFT of the exit-surface complex wave whose intensity and phase images are displayed in Fig. 3a. This map is corresponding to the local diffraction pattern for the rectangular area ABCD shown in Fig. 1a (the reason for the amplitude map rather than the intensity one of the FFT of the wave is merely to see weak spots more clearly). This diffraction pattern gives useful information such as the resolution limit and the exact orientation of the selected local area of the specimen. The amplitudes

Table 1. The crystallographic data of the model structure with the least-squares refinements. The *z*-coordinates of atoms are assumed to be the same as the data of the perfect crystal [10]

Atom	Site	*x/a*	*y/b*	*z/c*	Atom	Site	*x/a*	*y/b*	*z/c*
Si	1	0.163	0.403	0.75	N	1′	0.038	0.334	0.25
	2	0.400	0.241	0.25		2′	0.317	0.285	0.75
	3	0.229	0.826	0.75		3′	0.300	0.980	0.25
	4	0.827	0.594	0.25		4′	0.982	0.680	0.75
	5	0.603	0.770	0.75		5′	0.683	0.704	0.25
	6	0.763	0.165	0.25		6′	0.692	0.015	0.75
						7′	0.329	0.672	0.75
						8′	0.669	0.360	0.25

Space group, Triclinic P1 (No. 1).
Cell parameters, $a = b = 0.7604$ nm, $c = 0.2906$ nm, $\alpha = \beta = 90°$, $\gamma = 117.5°$.
The error range, 0.004 nm.

Table 2. Separations of atomic columns of the six-membered ring in the [0001] projected plane.

Si(1)–Si(2)–Si(3)–Si(4)–Si(5)–Si(6)–Si(1): 0.261–0.281–0.274–0.261–0.267–0.273 nm
<average> ± standard deviation: <0.269> ± 0.008 nm: (Si–Si: 0.268 nm)*
N(1′)–N(2′)–N(3′)–N(4′)–N(5′)–N(6′)–N(1′):
0.232–0.226–0.244–0.236–0.234–0.262 nm: <0.239> ± 0.013 nm : (N-N: 0.240 nm)*.
Si(1)–N(1′): 0.085 nm Si(2)–N(2′): 0.084 nm Si(3)–N(3′): 0.104 nm
Si(4)–N(4′): 0.105 nm Si(5)–N(5′): 0.096 nm Si(6)–N(6′): 0.101 nm
<0.096> ± 0.012 nm: (Si–N: 0.095 nm)*.

()*, the values calculated from the data of a perfect β-Si_3N_4 crystal [10]. The error range, 0.004 nm.

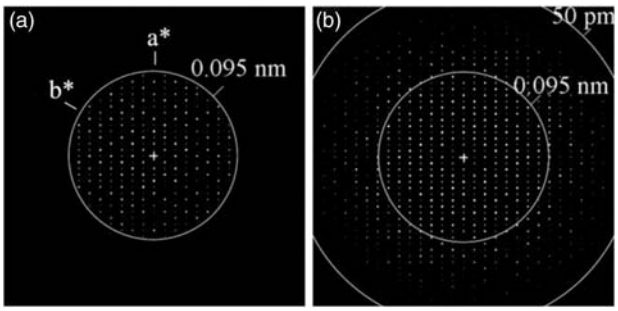

Fig. 4. (a) The amplitude map of FFT of the reconstructed exit-plane complex wave for Fig. 3a. This corresponds to the real diffraction pattern of the specimen area ABCD in Fig. 1a. Note that diffraction spots lie within the limit of ~1/(0.095 nm). (b) FFT of the intensity image of Fig. 3a. Fourier components extend up to ~1/(50 pm), just twice the limit in (a).

of the diffraction can also be used for the least-squares refinements of parameters of a model structure, as seen in the following sections.

Resolution limit

Figure 4a shows that all diffraction spots lie below $g_{max} \approx 1/(0.095\ \text{nm})$. This limitation, in fact, comes from the input parameter of the optimum cut-off value of the (mainly temporary) damping envelope function in the algorithm of the IWFR method, rather than the objective aperture limitation. This optimum value is set to 0.2. That is, for $\lambda = 1.968 \times 10^{-3}$ nm for 300 keV electron, the focal spread $\Delta_s = 2.9$ nm and $g_{max} = 10\ \text{nm}^{-1}$, the temporary damping envelope function $D(g_{max}) = \exp[-0.5\pi^2\lambda^2\Delta_s^2(g_{max})^4]$ 0.2. Diffraction vectors larger than $g_{max} = 10\ \text{nm}^{-1}$ (which give $D(g) \leq 0.2$) were ignored simply to obtain the best reconstructed exit-wave. $d_{min} = 1/g_{max}$ is considered to be the guaranteed resolution limit for our HRTEM images. In practice, the resolution of peaks in the image could be recognized up to $\sim 0.8 d_{min}$. In this case, two peak shapes increasingly overlapped and the separation of the peaks appeared to be reduced proportionally to the degree of overlapping [13]. In this experiment, the real separation of Si–N dumbbells is 0.095 nm, slightly less than $d_{min} = 0.1$ nm. Nevertheless in the image of Fig. 3b these separations are well resolved. Figure 4b is the FFT of the intensity of Fig. 3a, whose image Fourier components extend up to $\sim 1/(50\ \text{pm}) = 2g_{max}$. The intensity distribution in this FFT has mathematically an inverse symmetry (Friedel's law). This figure is similar to Fig. 1b, which is the FFT of Fig. 1a. Interestingly in the literature [8] the value of $(2g_{max})^{-1}$ is often considered to be the information (or resolution) limit. Recently, O'Keefe *et al.* [14,15] have criticized that this value is not a direct indication of atomic resolutions found in HRTEM images. Here, one should note that the correction of $D(\text{g})^{-1}$ essentially gives the better resolution intensity image in Fig. 3a than in the raw image in Fig. 1a. Besides, weak super cell spots can be seen in the FFT maps of Fig. 4. These spots are in fact artifacts, which should be ignored as they come from the second stage of image processing by averaging over the translation symmetry of a super cell.

The symmetry relation in the amplitudes

The amplitudes of the diffraction spots in Fig. 4a are listed in Table A1 in Appendix. And these amplitudes have no particular symmetry relation such as the hexagonal symmetry or the inverse symmetry (Friedel's law). Here, it is recalled that because the exit-wave was reconstructed from the images at the second stage image process as stated above, the reciprocal lattice in Fig. 4a (the FFT of the exit-wave) apparently shows a perfect hexagonal unit cell: but it should be viewed geometrically as the reciprocal lattice of the triclinic cell area ABCD in Fig. 1a, deviated about 2.5° from the hexagonal. The failure of Friedel's law, i.e. the inverse asymmetry in the amplitudes may arise under two situations in this experiment: one is due to the possible specimen mistilting to the beam direction, and the other due to the non-centrosymmetrical triclinic structure of the selected specimen area. It is reminded that Friedel's law does not hold for non-centrosymmetry crystal in electron diffractions [16]. The effects giving the failure of Friedel's law from these two situations on the diffraction can be distinguishable, however. For instance, ±(50.0) reflections show large asymmetry in the intensity; but the next ±60.0 reflections show just slightly reverse asymmetry (see also Table A1 in the appendix). This fact cannot be explained with specimen mistilting, and can only be understood by the violation of Friedel's law for non-centrosymmetry crystal. At the same time, an intensity gradient of the ensemble of spots from the upper left corner to the lower right corner in Fig. 4a indicates an evidence of small specimen mistilting effect.

A model structure with least-squares refinements

We are now interested to find a model structure which gives uneven resolutions of the dumbbells in the six-membered rings. For this purpose, the method of least-squares was employed with data of the diffraction amplitude of each reflection (Fig. 4a). The computer program based on the algorithm of nonlinear least squares fitting in Ref. [17] has been developed for this work. The function minimized was $\sum||\phi_g|^e - |\phi_g|^c|$ including the transmitted reflection of $g = 0$ with the normalization of $\sum|\phi_g|^2 = 1$ when no absorption was assumed. Here $|\phi_g|^e$ is the diffraction amplitude of **g**-reflection as in

Fig. 4a and Table A1 in the appendix, and $|\phi_g|^c$ is the calculated amplitude for a model structure. And the residual indices as fitting parameters are defined as

$$R_a = \frac{\sum ||\phi_g|^e - |\phi_g|^c|}{\sum |\phi_g|^e},$$

$$R_i = \frac{\sum |(|\phi_g|^e)^2 - (|\phi_g|^c|)^2|}{\sum (|\phi_g|^e)^2}$$

with 163 reflections under $\mathbf{g} < 10\ \mathrm{nm}^{-1}$. It should be noted that these amplitudes, in principle, are not relevant to residual aberrations, because the exit-surface wave itself is free from such optical parameters causing aberrations. As a characteristic feature of the uneven resolutions, the separations of intensity peaks of the dumbbells in the ring in Fig. 5a, which is an enlarged part of Fig. 3a, are measured: Si(1)–N(1′): 0.090 nm; Si(2)–N(2′): 0.078 nm; Si(3)–N(3′): 0.112 nm; Si(4)–N(4′): 0.099 nm; Si(5)–N(5′): 0.082 nm; Si(6)–N(6′): 0.099 nm (the error in measurement: ~0.004 nm), whereas the atomic column separation of the Si–N dumbbell is 0.095 nm in the [0001] projection of a perfect β-Si_3N_4.

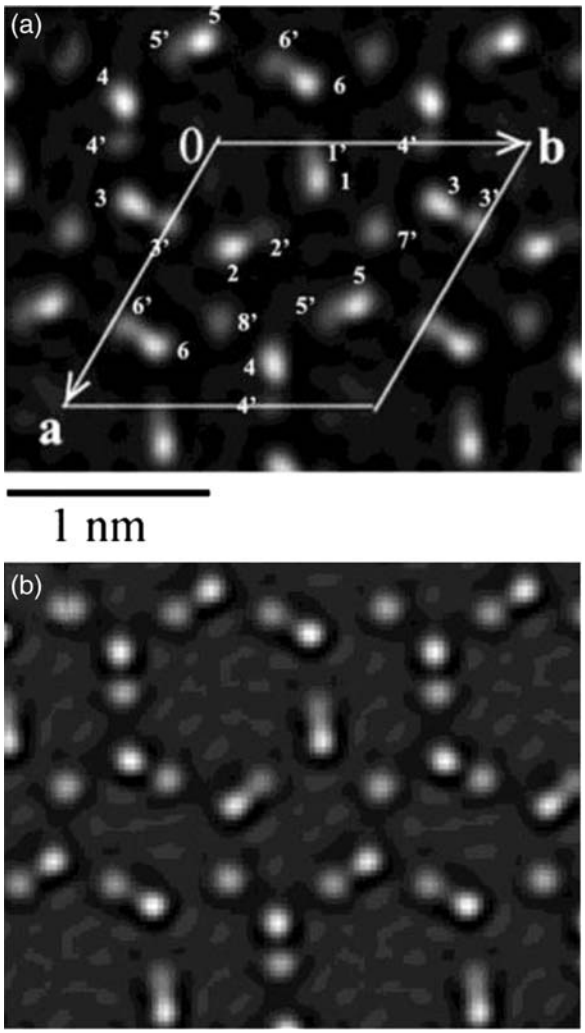

Fig. 5. (a) The enlarged part of Fig. 3a, the intensity image of the exit-surface wave. The triclinic unit cell is drawn, and the sites of nos. 1–6 are for Si atom columns and those of prime nos. 1′–8′ are for N atom columns used for atomic sites listed in Table 1. (b) the corresponding simulated image with the model refined finally, the enlarged part of Fig. 7a.

Results

For the specimen mistilting and/or beam tilting (coma)

Let us first explore the possibility that uneven resolutions of the dumbbells in the six-membered rings might come only from the specimen mistilted and/or beam tilting (coma), whose structure is still a perfect hexagonal symmetry crystal [9,10]. For this case, it is good enough to refine the parameters of the specimen thickness (t), the angle tilted (θ) in a certain direction and temperature factor (B). Please note again that the data of amplitudes in Table A1 are independent of the optical parameters such as the coma in principle. For the initial parameters, $t = 5$ nm, $\theta = 0°$ and $B = 1.0 \times 10^{-2}$ nm^2 for all atoms, $R_a = 28.8\%$ and $R_i = 27.1\%$ were calculated. After the refinements $R_a = 23.5\%$ and $R_i = 15.4\%$ were obtained with $t = 5.7$ nm, $B_{Si} = 0.2 \times 10^{-2}$ nm^2, $B_N = 0.7 \times 10^{-2}$ nm^2 and $\theta = 5.2$ mrad (0.3°) in *[32.0]** direction: $K_x = -0.4$[32.0]*. But the intensity image with this data showed no significant difference from the image of a perfect crystal with [0001] orientation exactly. Further to make the image similar to Fig. 5a, it was assumed that a large second-order coma $B_2 = 250$ nm (the coma axis: $\sim -\pi/4$ from *[h0.0]**) is additionally associated with the above exit-wave calculated from 0.3° mistilted specimen at the image plane. The resulting image simulated is displayed in Fig. 6a. In this simulated image the separations of peaks of Si–N dumbbells in the rings merely are measured as ~0.095 nm or less, not matched with the characteristic feature of the uneven resolutions showing in Fig. 5a. Still, we have tried to see if a large specimen mistilted image could be matched

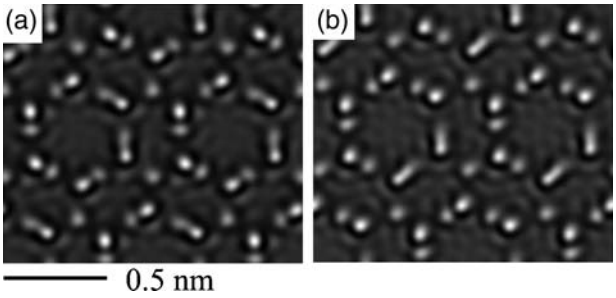

Fig. 6. (a) The simulated image under the conditions of 5.2 mrad specimen mistilting in the [32.0]*-direction and the axial coma of B_2 = 250 nm. (b) the simulated image with the tilting angle of 0.75° (13.1 mrad) in the [5–2.0]*-direction. $C_s = \Delta f = 0$ were given in calculations with $\gamma = 120°$ for the lattice cell.

with Fig. 5a, apart from the work of the least-squares fitting. Figure 6b shows the best resemble image with Fig. 5a, simulated with the tilting angle $\theta = 13.1$ mrad (0.75°): $K_x = -[5\text{–}2.0]^* = 6.63\ \text{nm}^{-1}$. It is noted that the magnitude of this angle is close to 10**g** (**g** = *10.0*) Bragg diffraction angle! Also the diffraction amplitudes of this image gave quite large residual indices, $R_a = 31.5\%$ and $R_i = 25.3\%$. Again the separations of peaks of Si–N dumbbells in the rings also are measured as ~0.095 nm or less, not matched with Fig. 5a. Above all, it is quite clear that a moderate crystal mistilt and/or residual aberrations could not give a distorted lattice image with ~2.5° deviation from the hexagonal! Therefore, we have to relax the condition of a perfect hexagonal structure in the least-squares refinements for a model structure.

For a triclinic model structure

For a triclinic cell structure of the model the atomic coordinates for a perfect crystal in the plane perpendicular to the [0001]-direction, with 28 parameters of x and y for 14 atoms (6Si and 8N) in the unit cell, were relaxed in the least-squares refinements while keeping the parameters: $t = 5.7$ nm, $B_{Si} = 0.2 \times 10^{-2}$ nm^2, $B_N = 0.7 \times 10^{-2}$ nm^2 and $\theta = 5.2$ mrad (0.3°) in the *[32.0]** direction previously obtained above. In this process, the coordinates of the triclinic cell model (with $\gamma = 120.0°$, not $\gamma = 117.5°$) was refined for a convenience. This procedure can be justified from the fact that since the deviation of the angle of 2.5° is small, the changes in the atomic positions in the cell coordinates are insignificantly small when the cell frame with $\gamma = 120.0°$ is transferred to the real triclinic cell with $\gamma = 117.5°$ and vice versa.

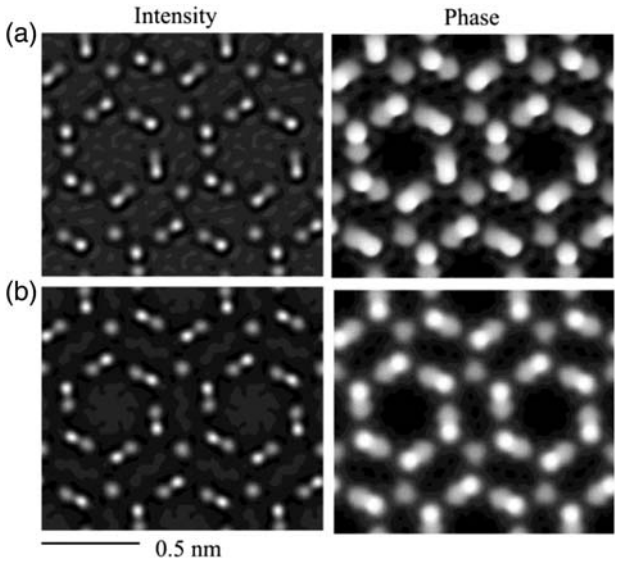

Fig. 7. (a) The simulated intensity and phase images for the refined model structure in Table 1 and (b) the averaged ones with $C_s = \Delta f = 0$, $\gamma = 120°$ for the lattice cell.

The result of the refinements gives $R_a = 20.4\%$ and $R_i = 13.6\%$. The data of the refined atomic coordinates are listed in Table 1, and the diffraction amplitudes of 163 reflections, calculated with the data, are listed in Table A1. Table 2 lists the separations of atomic columns of a six-membered ring in the (0001) plane. The distances of the separation are generally in agreement with the measured separations from Fig. 5a: the differences of separations of Si–N dumbbells between those in Table 2 and the measured ones stated above are 0.005, 0.006, –0.008, 0.006, 0.014, 0.002 nm in order. Since the measurement error is ~0.004 nm, this discrepancy is considered insignificant, except 0.014 nm of Si(5)–N(5). The simulated images of the intensity and the phase, and their averaged images are as shown in Fig. 7. These images are reasonably well matched with those of Fig. 3a and b. It should be noted that the simulations are independent of z-coordinates of atoms in the model, which is unknown, because the images are the projected ones along the z-[0001]-direction.

For Si–N bond lengths in SiN_4 tetrahedrons

To see further whether the refined (x, y) positions of the atoms (Table 1) are physically reasonable, calculations of the Si–N bond length were carried out with the z-coordinates assumed to be those of the perfect structure of β-Si_3N_4 as listed in Table 1. The crystal structure of β-Si_3N_4 basically consist of

three corner-sharing SiN_4 tetrahedrons. Therefore, only the variation in the bond lengths of the tetrahedrons of the triclinic model was calculated (Table 3). As seen in this table, the variation in bond lengths lies in the range of 0.163–0.192 nm with the averaged value 0.176 nm. This 0.176 nm is, within the measurement error of 0.004 nm, consistent with the almost fixed length of 0.173–0.174 nm in a perfect crystal [9,10]. For comparison, we have noted that in α-Si_3N_4 the variation of the tetrahedral bond lengths of Si–N (4) is reported to be from 0.164 to 0.193 nm [18], which is quite close to those in this case. It is well known that α-Si_3N_4 consists essentially of alternate basal layers of β-Si_3N_4 [9]. In light of this fact, we consider that this bond length variation in SiN_4 tetrahedrons can be quite acceptable physically.

Finally, the simulated images for the triclinic model structure data with $\gamma = 117.5°$ in Table 1, corresponding to the original raw images in Fig. 2a are shown in Fig. 8. The agreement between simulations and the observed images is striking. Here it is emphasized that the triclinic crystal data in Table 1 are only for the specimen area of 4×4 cells in the rectangular ABCD, not for the full specimen area in Fig. 1a. In fact, a careful measurement of cell parameter variation over 7×7 cells (49 cells) in Fig. 1a gives that $a = 0.766 \pm 0.010$ nm, $b = 0.755 \pm 0.010$ nm, $\gamma = 118.14° \pm 2.27°$. This means that the Si–N bond lengths in SiN_4 tetrahedrons are changed slightly from cell to cell also. This variation will be responsible for forming a not well-defined (reciprocal) lattice arrays shown in Fig. 1b.

Thickness dependence of the asymmetry of images

On the other hand, the HRTEM image and its FFT in Fig. 9 show that the deviation from the hexagonal lattice symmetry is reduced in this case within ~1.5°, as compared with 2.5°–3° in Fig. 1. The image here (Fig. 9a) was taken from a relatively thick area (~7 nm) of the same sample. Interestingly, in the literature [2,4,19], a similar asymmetry was noted by us in the reported HRTEM images for β-Si_3N_4 specimen with a thickness of ~7 nm. In the reported HRTEM images, the degree of the asymmetry was measured to be about 1.1°. These results indicate that the degree of asymmetry decreases with increasing thickness of the specimen. This dependency could be explained as within a thicker crystal the stress of this bond length variation would cause higher crystal energy, and then the rearranging positions of atoms making a fixed bond length of ~0.173 nm would reduce the energy. Thus, the images of specimens with thickness larger than 10 nm would show increasingly the hexagonal lattice symmetry for the bulk crystal of β-Si_3N_4 (determined by X-rays).

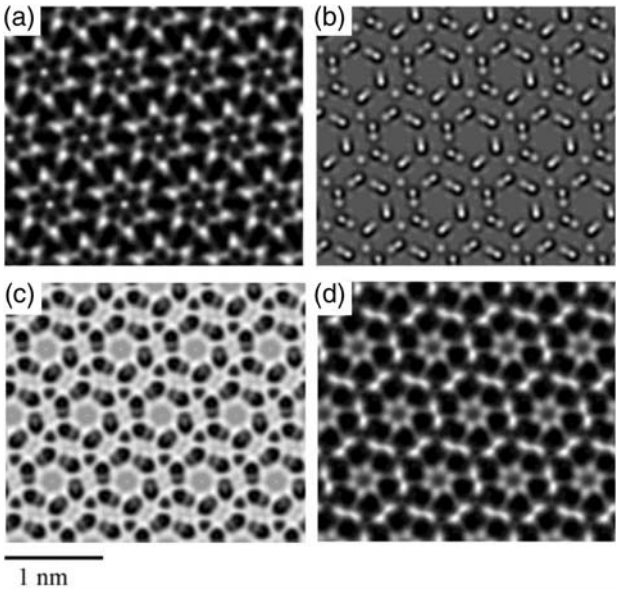

Fig. 8. Simulated images with the triclinic model structure in Table 1. These images correspond to the experimental images in Fig. 2a as follows: (a) $\Delta f = +31.0$ nm, (b) $\Delta f = -0.7$ nm, (c) $\Delta f = -6.0$ nm and (d) $\Delta f = -11.5$ nm.

Table 3. Bond lengths (nm) in Si–:N_4 tetrahedrons of the model structure in Table 1.

Si(1) – 2N(1′): 0.168	Si(2) – 2N(2′): 0.168	Si(3) – 2N(3′): 0.179
– N(2′): 0.178	– N(3′): 0.177	– N(4′): 0.169
– N(7′): 0.184	– N(8′): 0.181	– N(7′): 0.166
Si(4) – 2N(4′): 0.179	Si(5) – 2N(5′): 0.174	Si(6) – 2N(6′): 0.177
– N(5′): 0.165	– N(6′): 0.166	– N(1′): 0.188
– N(8′): 0.163	– N(7′): 0.186	– N(8′): 0.192

Average bond length of Si–N and the standard deviation: 0.176 nm ± 0.009 nm (0.173 ~ 0.174 nm for a perfect crystal [9]). The error range: 0.004 nm.

Discussion

In an aberration-corrected HRTEM image of β-Si_3N_4 [0001] (Fig. 1) presented in Ref. [1] not all dumbbells in the six-membered rings are evenly resolved.

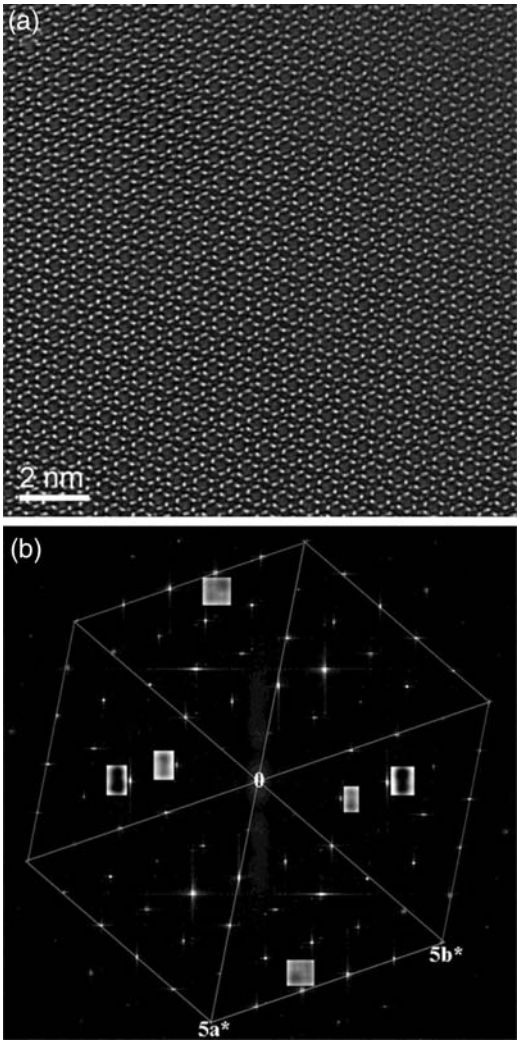

Fig. 9. (a) HRTEM image of β-Si_3N_4[0001] acquired under $C_s = 10$ μm at the defocus −3 nm for a ∼7 nm thick sample area (the same as Fig. 7 in [1]), (b) FFT of (a). In (b), a hexagon with equilateral triangles is drawn to see clearly the deviation of the reciprocal lattice spots from the hexagonal. The splitting spots in insets corresponding to the nearest spots are enlarged five times for clarity. The splitting angle of these spots is ∼1.5°. $|5a^*| = |5b^*| = 1/(0.132\ \text{nm})$.

In this work, we find that this observation is basically not relevant to specimen bending or/and slight mis-orientation of specimen or/and residual aberrations. This turns out to be due to an asymmetry structure with a distorted lattice, roughly deviated by ∼2.5° from the hexagonal lattice. We find that the local structure is triclinic (see Table 1) and the tetrahedral bond length of Si–N(4) varies from ∼0.163 to ∼0.192 nm with an average of 0.176 nm (see Table 3). This variation gives the uneven separation of dumbbells of Si–N in the six-membered rings in the [0001] projection, from ∼0.084 to ∼0.105 nm with the average of 0.096 nm (see Table 2). Therefore, the resolution limit of ∼0.08 nm (the guaranteed resolution, 0.1 nm) of our microscope used in the experiment of Ref. [1] does not allow resolving all the dumbbells with equal accuracy. That is, in Fig. 5a the separation of Si(3)–N(3) is 0.104 nm and is shown to be well resolved, but the separations of Si(1)-N(1) and Si(2)-N(2) are near the edge of the microscope's resolution limit of 0.08 nm, and hence are not resolved well. Here, it should be emphasized that the model structure in Table 1 is only one of all other possible local structures with an irregular asymmetry. That is, other variations may occur from region to region in the entire specimen.

Origin of the asymmetry structure of a thin β-Si_3N_4 [0001] crystal

This study indicates that the local structural variation prevails only in a thin specimen. This fact naturally predicts that the near surface structure of β-Si_3N_4 [0001] should exhibit the same type of disorder of local symmetry breaking. Relating to this expectation we have noticed the reported images of β-Si_3N_4 [0001] in Ref. [20] by a scanning transmission electron microscope (STEM). These images are the bright field and annular dark field ones. Interestingly, the lattices of these images were measured to be ∼2° deviations from a perfect hexagonal lattice, like the image in Fig. 1a (Kimoto *et al.* [20] seem not to have noticed this aspect). In general, STEM images are known to have come from scatterings at a certain surface depth (perhaps less than a few nanometers) of the specimen. One might doubt that the 2° deviations in the images may be due to a drift in STEM. However, these images have been taken by a highly stabilized STEM. The demonstration of this stability can be seen in another STEM images of [110] silicon in Fig. 2 in the same paper, noting that the images show no significant drift. Further, in the study of clean Si_3N_4 surface reported in Ref. [21], the paper states in Section 3.3 that 'No low-energy electron diffraction pattern was seen, not even a (1×1) pattern from the bulk of the film, which indicates that the Si_3N_4 LPCVD films are disordered. Since no ion bombardment was done, this disorder appears to be intrinsic to the present films and not the

result of damage incurred during surface cleaning'. Generally, the low-energy electron diffraction comes only from scatterings by a few atomic layers of the surface. Thus the reported disorder may be for the structure of a few atomic layers of the surface and then could be explained with the Si–N bonding variation discussed above. Furthermore, in the theoretical study for the structure of a Si_3N_4 film growth along the [0001] crystal direction during chemical vapor deposition (CVP) in Ref. [22], this paper states in conclusions that 'the dangling bonds on the bare surface are relaxed, and the calculated Si = N bond length 0.161 nm is considerably shorter than typical lengths of crystalline Si–N bonds (0.174–0.176 nm), and the surface atoms of these diatomic groups are significantly displaced from the bulk crystalline positions'. This bond length of 0.161 nm is very close to the shortest distance of 0.163 nm in Si–N tetrahedrons listed in Table 3. With all these evidences reported in the literature [4,19–22], we can conclude with confidence that a local structural variation shown in a thin β-Si_3N_4 [0001] could not be certain artifacts that are being produced either by distortions of the microscope imaging system or by a residual beam tilt and/or as a result of crystal damage—by either during thinning of an ion beam or the electron beam (including surface charging) upon imaging, but is an intrinsic property of Si–N bond length variation in SiN_4 tetrahedrons in the crystal structure. It is emphasized again that such artifact images could not have a distorted lattice apparently 2°–2.5° deviated from the perfect hexagonal cell as observed in Fig. 1a and as being reported in Refs. [4,19,20]. Generally speaking, the artifact damage during the specimen preparation due to ion bombardments, etc. is supposed to make statistical random distribution of possibly various defects such as point defect, dislocation, stacking fault, etc. on the specimen over a relatively large area of μm size, and are observable in the HRTEM image too. Please note that the area of Fig. 1 is less than ~7 nm × 7 nm. And these kinds of defects have not been observed in Fig. 1. As another possibility, if intermixing of O atoms in the Si_3N_4 lattice occurs significantly due to inclusion of oxygen atoms during the β-Si_3N_4 grain growth, then this mixing would certainly make the variation in the Si–N bond length and/or could even destroy the SiN_4 tetrahedron configuration; however, the average of this bond length variation gives very unlikely the fixed length of a bulk of β-Si_3N_4 and the resulting structure of the lattice would not show even a distortion deviated slightly from the hexagonal. Thus, we can exclude this possibility for the asymmetry observation in Fig. 1a. Finally, during this work we were aware of a conference report by Svete and Mader [23]: they have examined a 4.7 nm thick β-Si_3N_4 [0001] HRTEM images under (C_s-corrected) a FEI Titan (80–300) at 300 kV and $C_s = -13$ μm. The image at the defocus of +6 nm in [Fig. 1 single image] in the paper also shows the uneven resolution of dumbbells of Si–N in the six-membered rings. And they have explained this uneven resolution due to specimen tilting imaging. They have shown by matching images with the simulation performed with the structure of perfect β-Si_3N_4 at a crystal tilt of $t_x = 0.5°$ (tilt axis parallel to horizontal edge of image) and $t_y = 0.6°$ (tilt axis parallel to horizontal edge of image). No beam tilt (axial coma) or others was applied in the simulations. Because this study is very close to our case, we have carefully reexamined all images with the reported data in the paper. Indeed, the lattice of the single image of Fig. 1 (observed) shows no significant deviation from the hexagonal cell. However, we have noticed by careful measurement that the phase and the amplitude images of the reconstructed exit-wave shown in Fig. 2 and the modulus of the Fourier transformed exit-plane wave (FT of EPW of Fig. 1) in the same paper clearly show distortion lattice images of the 2°–2.5° deviations from the perfect hexagonal cell. This result is inconsistent with Fig. 1 (single image) showing a good hexagonal lattice image. Moreover, the separations of intensity peaks of the dumbbells in the six-membered rings in the image are from 0.108 to 0.054 nm, while in the simulated image inset the separations are 0.095 nm or ≤0.081 nm as expected. The separation of 0.108 nm (more than 0.095 nm) cannot be obtained by the specimen tilting of the perfect crystal with true separation 0.095 nm in the [0001] projection, mathematically. Therefore, it is unclear that their experiment results can be explained reasonably by the mere specimen tilting.

Concluding remarks

Careful examination of the uneven resolution of dumbbells in the six-membered rings observed in HRTEM image of a thin [0001] β-Si_3N_4 reveals an intrinsic property of the certain variation of Si–N bond length in SiN_4 tetrahedron. Also this variation seems to be responsible for forming a not well-defined crystal of β-Si_3N_4 with slightly distorted lattice, apparently 2°–2.5° deviated from the perfect hexagonal cell, as the thickness is thin, such as ~5–6 nm. However, the average of the tetrahedral Si–N(4) bond length variation is close to the fixed length known in the bulk crystal of β-Si_3N_4.

References

1 Zhang Z L and Kaiser U (2009) Structure imaging of β-Si_3N_4 by spherical aberration-corrected high-resolution transmission electron microscopy. *Ultramicroscopy* **109**: 1114–1120.

2 Allen L J, McBride W, O'Leary N L, and Oxley M P (2004) Exit wave reconstruction at atomic resolution. *Ultramicroscopy* **100**: 91–104.

3 Allen L J, Oxley M P, and Ishizuka K (2006) Electron microscope C_s correction using iterative wave-function reconstruction. *Microsc. Anal.* **52**: 5–7.

4 Kim H S (2010) Atomic resolution improvement by a new method using the second derivative of the intensity function of the reconstructed exit wave of electrons for a thin β-Si_3N_4 crystal. *Scripta Mater.* **63**: 524–527.

5 Hirsch P, Howie A, Nicholson R B, Pashley D W, and Whelan M J (1977) *Electron Microscopy of Thin Crystals* (Krieger, Huntington, NY).

6 Lentzen M (2006) Progress in aberration-corrected high-resolution transmission electron microscopy using hardware aberration correction. *Microsc. Microanal.* **12**: 191–205.

7 Lehmann M and Lichte H (2002) Tutorial on off-axis electron holography. *Microsc. Microanal.* **8**: 447–466.

8 Kisielowski C, Freitag B, Bischoff M, van Lin H, Lazar S, Knippels G, Tiemeijer P, van der Stam M, von Harrach S, Stekelenburg M, Haider M, Uhlemann S, Müller H, Hartel P, Kabius B, Miller D, Petrov I, Olson E A, Donchev T, Kenik E A, Lupini A, Bentley R J, Pennycook S J, Anderson I M, Minor A M, Schmid A K, Duden T, Radmilovic V, Ramasse Q M, Watanabe M, Erni R, Stach E A, Denes P, and Dahmen U (2008) Detection of single atoms and buried defects in three dimensions by aberration-corrected electron microscope with 0.5-Å information limit. *Microsc. Microanal.* **14**: 469–477.

9 Grün R (1979) The crystal structure of β-Si_3N_4; structural and stability considerations between α- and β-Si_3N_4. *Acta Crystallogr. B* **35**: 800–804.

10 du Boulay D, Ishizawa N, Atake T, Streltsov V, Furuya K, and Munakata F (2004) Synchrotron X-ray and *ab initio* studies of β-Si_3N_4. *Acta Crystallogr. B* **60**: 388–405.

11 Hÿtch M J and Stobbs W M (1994) Quantitative comparison of high resolution TEM images with image simulations. *Ultramicroscopy* **53**: 191–203.

12 Thust A (2009) High-resolution transmission electron microscopy on an absolute contrast scale. *Phys. Rev. Lett.* **102**: 220801–220804.

13 O'Keefe M A (2008) Seeing atoms with aberration-corrected sub-Ångström electron microscopy. *Ultramicroscopy* **108**: 196–209.

14 O'Keefe M A, Allard L F, and Blom D A (2008) Young's fringes are not evidence of HRTEM resolution. *Microsc. Microanal.* **14** (Suppl. 2): 834–835.

15 O'Keefe M A, Allard L F, and Blom D A (2009) Defining HRTEM resolution: why Young's fringes don't determine resolution. *Microsc. Microanal.* **15** (Suppl. 2): 1470–1471.

16 Serneels R, Snykers M, Delavignette P, Gevers R, and Amelincks A (1973) Friedel's law in electron diffraction as applied to the study of domain structures in non-centrosymmetrical crystals. *Phys. Stat. Sol. (b)* **58**: 277–292.

17 DeVries P L (1994) *A First Course in Computational Physics*, pp. 138–143 (Wiley, New York).

18 Yang P, Fun H K, Rahman I A, and Saleh M I (1995) Two phase refinements of the structures of α-Si_3N_4 and β-Si_3N_4 made from Rice Husk by Rietveld analysis. *Ceramics Int.* **21**: 137–142.

19 Ziegler A, Kisielowski C, and Ritchie R O (2002) Imaging of the crystal structure of silicon nitride at 0.8 Ångström resolutions. *Acta Mater.* **50**: 565–574.

20 Kimoto K, Nakamura K, Aizawa S, Isakozawa S, and Matsui Y (2007) Development of dedicated STEM with high stability. *J. Electron Microsc.* **56**: 17–20.

21 Bermudez V M and Perkins F K (2004) Preparation and properties of clean Si_3N_4 surfaces. *Appl. Surf. Sci.* **235**: 406–419.

22 Bagatur'yants A A, Novoselov K P, Safonov A A, Cole J V, Stoker M, and Korkin A A (2001) Silicon nitride chemical vapor deposition from dichlorsilane and ammonia: theoretical study of surface structures and reaction mechanism. *Surf. Sci.* **486**: 213–225.

23 Svete M and Mader W (2008) Quantitative HRTEM studies of reconstructed exit-plane waves retrieved from C_s-corrected electron microscopes. In: European Microscopy Conference (EMC'08), Aachen, Germany, September 1–5, 2008, Vol. 1, pp. 159–160.

Appendix

Table A1. Diffraction amplitudes ($|\phi_g|^e$) of Fig. 4a, derived from the reconstructed exit-wave and calculated ones ($|\phi_g|^c$) for the crystal structure in Table 1, with a thickness of $t = 5.68$ nm and $\theta = 5.2$ mrad for the specimen mistilt ($R_a = 20.4\%$ and $R_i = 13.6\%$)

h	k	$\lvert\phi_g\rvert^e$	$\lvert\phi_g\rvert^c$	h	k	$\lvert\phi_g\rvert^e$	$\lvert\phi_g\rvert^c$	h	k	$\lvert\phi_g\rvert^e$	$\lvert\phi_g\rvert^c$	h	k	$\lvert\phi_g\rvert^e$	$\lvert\phi_g\rvert^c$
0	0	0.764	0.767	–2	4	0.048	0.026	4	–5	0.035	0.032	6	0	0.030	0.026
				2	–4	0.028	0.035	–5	4	0.042	0.033	–6	0	0.033	0.013
1	0	0.032	0.032	–4	2	0.030	0.035	5	–4	0.042	0.050	0	6	0.050	0.025
–1	0	0.036	0.036	4	–2	0.047	0.049	–5	1	0.039	0.031	0	–6	0.032	0.012
0	1	0.034	0.035					5	–1	0.055	0.049	–6	6	0.031	0.025
0	–1	0.034	0.043	3	1	0.051	0.056					6	–6	0.024	0.018
–1	1	0.037	0.032	–3	–1	0.028	0.051	5	0	0.029	0.037				
1	–1	0.032	0.037	1	3	0.027	0.029	–5	0	0.002	0.022	4	3	0.014	0.018
				–1	–3	0.018	0.018	0	5	0.040	0.049	–4	–3	0.007	0.007
1	1	0.070	0.079	–1	4	0.061	0.056	0	–5	0.009	0.024	3	4	0.061	0.060
–1	–1	0.065	0.071	1	–4	0.035	0.053	–5	5	0.024	0.030	–3	–4	0.031	0.013
–1	2	0.085	0.072	–3	4	0.029	0.030	5	–5	0.018	0.021	–3	7	0.013	0.008
1	–2	0.060	0.062	3	–4	0.012	0.014					3	–7	0.025	0.016
–2	1	0.081	0.069	–4	3	0.051	0.058	3	3	0.068	0.072	–4	7	0.048	0.035
2	–1	0.061	0.070	4	–3	0.052	0.067	–3	–3	0.032	0.034	4	–7	0.017	0.021
				–4	1	0.020	0.024	–3	6	0.070	0.056	–7	4	0.019	0.006
2	0	0.139	0.128	4	–1	0.016	0.025	3	–6	0.058	0.045	7	–4	0.020	0.022
–2	0	0.121	0.124					–6	3	0.042	0.041	–7	3	0.032	0.019
0	2	0.152	0.118	4	0	0.011	0.016	6	–3	0.052	0.064	7	–3	0.043	0.040
0	–2	0.097	0.107	–4	0	0.012	0.010								
–2	2	0.141	0.121	0	4	0.010	0.011	4	2	0.013	0.013	5	2	0.025	0.022
2	–2	0.114	0.119	0	–4	0.006	0.013	–4	–2	0.014	0.010	–5	–2	0.010	0.004
				–4	4	0.011	0.006	2	4	0.028	0.026	2	5	0.008	0.011
2	1	0.013	0.014	4	–4	0.012	0.016	–2	–4	0.015	0.009	–2	–5	0.035	0.007
–2	–1	0.003	0.009					–2	6	0.015	0.004	–2	7	0.024	0.023
1	2	0.158	0.133	3	2	0.062	0.065	2	–6	0.010	0.002	2	–7	0.025	0.007
–1	–2	0.097	0.116	–3	–2	0.023	0.042	–4	6	0.029	0.029	–5	7	0.019	0.006
–1	3	0.020	0.021	2	3	0.063	0.068	4	–6	0.018	0.018	5	–7	0.035	0.011
1	–3	0.008	0.016	–2	–3	0.020	0.043	–6	4	0.010	0.008	–7	5	0.012	0.016
2	–3	0.120	0.140	–2	5	0.082	0.073	6	–4	0.007	0.008	7	–5	0.012	0.011
–2	3	0.164	0.146	2	–5	0.034	0.060	–6	2	0.007	0.011	–7	2	0.014	0.003
3	–2	0.006	0.011	–3	5	0.063	0.051	6	–2	0.022	0.025	7	–2	0.036	0.012
–3	2	0.008	0.008	3	–5	0.039	0.047								
–3	1	0.129	0.129	–5	3	0.050	0.051	5	1	0.034	0.035	6	1	0.014	0.029
3	–1	0.139	0.136	5	–3	0.053	0.064	–5	–1	0.019	0.014	–6	–1	0.006	0.009
				–5	2	0.037	0.044	1	5	0.021	0.038	1	6	0.025	0.020
3	0	0.071	0.086	5	–2	0.058	0.063	–1	–5	0.014	0.016	–1	–6	0.005	0.005
–3	0	0.046	0.062					–1	6	0.043	0.019	–1	7	0.050	0.033
0	3	0.067	0.077	4	1	0.037	0.039	1	–6	0.031	0.018	1	–7	0.005	0.011
0	–3	0.031	0.061	–4	–1	0.020	0.024	–5	6	0.021	0.022	–6	7	0.034	0.010
–3	3	0.061	0.067	1	4	0.058	0.061	5	–6	0.009	0.019	6	–7	0.012	0.010
3	–3	0.047	0.078	–1	–4	0.033	0.029	–6	5	0.028	0.015	–7	6	0.008	0.016
				–1	5	0.054	0.044	6	–5	0.041	0.027	7	–6	0.036	0.023
2	2	0.047	0.051	1	–5	0.028	0.039	–6	1	0.012	0.013	–7	1	0.008	0.004
–2	–2	0.011	0.043	–4	5	0.044	0.045	6	–1	0.009	0.027	7	–1	0.014	0.012